Author/s:
Cao, Y;Zu, L;Du, X;Franks, GV;Liang, Q;Li, D

Title:
Solvent Effect on the Nanotextural Formation of Reduced Graphene Oxide Membranes

Date:
2023-10-18

Citation:
Cao, Y., Zu, L., Du, X., Franks, G. V., Liang, Q. & Li, D. (2023). Solvent Effect on the Nanotextural Formation of Reduced Graphene Oxide Membranes. Langmuir, 39 (43), pp.15260-15267. https://doi.org/10.1021/acs.langmuir.3c01957.

# Solvent Effect on the Nanotextural Formation of Reduced Graphene Oxide Membranes

*Yang Cao,[1] Lianhai Zu,[1] Xiaoyang Du,[1] George V. Franks,[1] Qinghua Liang [1,2,]* and Dan Li [1,]**

[1]Department of Chemical Engineering, University of Melbourne, Parkville, Victoria 3010, Australia.

[2]Key Laboratory of Rare Earths, Ganjiang Innovation Academy, Chinese Academy of Sciences, Ganzhou, Jiangxi 341000, China.

Corresponding Author

*E-mail: qhliang@gia.cas.cn; dan.li1@unimelb.edu.au

ABSTRACT

Solvent is involved in many wet-chemical synthesis and bottom-up assembly processes. Understanding its influences in the nanotextural formation of the resultant assemblies is essential for the design and control of the properties for targeted applications. With wet-chemically reduced graphene oxide (rGO) membranes as a materials platform, this study investigates the solvent effect on the nanotexture formation in 2D nanomaterial-based membranes through light scattering and electrochemical characterization. Our finding indicates that the nanotexture of the resultant rGO membrane is largely correlated to the dielectric constant of the solvent. Specifically, solvents with

higher dielectric constant yield rGO membranes with more wrinkled, loosely stacked, and less graphitized structures. In contrast, solvents with lower dielectric constant tend to yield densely stacked structures with larger graphitized domains. Our finding underscores the important role of solvents in wet processing and nanoengineering of 2D nanomaterial-based membranes and provides valuable insights for their controlled synthesis and application.

**KEYWORDS**. 2D laminar membranes, Nanostructures, Small-angle X-ray scattering, Solvent effect, Graphitic stacking.

## Introduction

2D nanomaterial-based membranes have emerged as versatile materials platforms for numerous applications, including energy conversion and storage, and ion separation, owing to their exceptional electronic and ionic conductivities.[1–3] To realize the desired performance in such on-demand applications, controlling the interlayer nanotextures of 2D laminar membranes is of paramount importance. Among the various designs and fabrication methods of 2D laminar membranes, wet-chemically produced 2D nanosheets are particularly intriguing as building blocks due to their cost-effectiveness, scalability, and modular configuration and interactions for various wet-chemical processing, including assembling, functionalization, and chemical treatment.[4] One exemplary method for producing graphene membranes is through the wet-chemical reduction of graphene oxide (GO) membranes, where the hydroiodic acid (HI) reduction method is widely employed.[5,6] While previous studies have devoted to understanding and controlling reduction conditions, such as temperature, time, and the type and concentration of chemical agents, to achieve the desired interlayer structure of the graphene membrane primarily in an aqueous solution,[7,8] the influence of solvents employed in wet-chemical reduction has yet to be explored.

From the viewpoint of colloid chemistry, the solvent, as an essential participant in wet-chemical processes, plays a pivotal role in determining the architectures of assemblies by mediating the conformation and colloidal interactions of the solvated building blocks.[9] In the context of 2D nanomaterials, the solvent effect is assumed to be more significant due to their relatively low bending stiffness compared to nanomaterials in other forms, such as nanodots and nanowires, rendering them more susceptible to the surrounding environment.[10] For example, the corrugation behavior of graphene nanosheets can be significantly influenced by the solvent nature, ranging from highly wrinkled, collapsed conformation to relatively flat extended conformation.[11,12] Furthermore, solvents could alter the interactions of two building blocks at the nanoscale, as reflected by the changed interlayer spacing of GO membrane in different types of solvents.[13,14] The surface interaction modulated by solvent can further assist the self-assembly of two molecules in a hybrid material system.[15] Given that numerous wet-chemical processes are employed to fabricate 2D nanomaterial-based membranes,[16] investigating the influence of solvents on nanotexture formation is crucial for not only developing controllable structural engineering approach but also optimizing the performance of these materials, yet remains largely unexplored.

In this study, we studied the impact of solvents on the nanotextural formation of wet-chemically produced 2D laminar membranes by conducting a systematic analysis of the HI-reduction of GO membranes in various solvents, including water, ethanol, and their mixtures. Our investigation with small-angle X-ray scattering (SAXS) and electrochemical measurements reveals that the rGO membrane reduced in water exhibited a more wrinkled, loosely stacked, and less graphitized structure compared to that reduced in ethanol. Further experiments with acetone and mixtures of water and ethanol indicate that solvent polarity is likely to be one of the determining factors for such solvent effects on nanotexture formation. This work not only demonstrates a significant

influence of the solvent on the nanotexture formation during the wet-chemical processing but also provides a strategy for engineering the nanostructure of 2D laminar membranes.

**Results and Discussion**

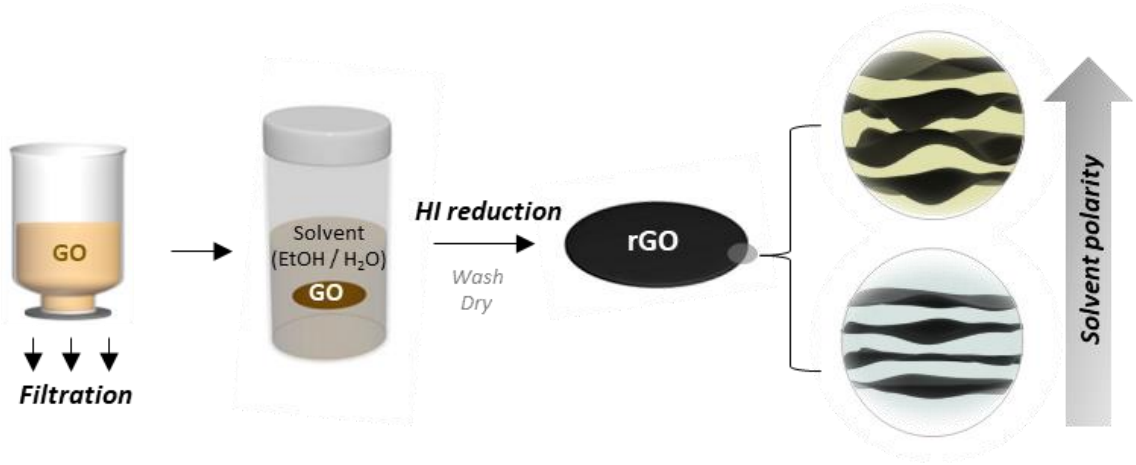


**Figure 1.** Illustration for the reduction of GO membrane in different solvents.

The reduced graphene oxide (rGO) membranes were prepared by directly reducing the vacuum-filtrated GO membrane with HI solution in different solvents (Figure 1). The GO nanosheets used in this work have a mean flake size of 1.33 $\mu m^2$ and a thickness of ~1 nm (Figure S1 and S2). We used water and ethanol to carry out the reduction as two solvents were commonly used in previous studies.[17,18] Before reduction, the vacuum-filtrated GO membrane (Figure S3) was respectively pre-immersed in Milli-Q water and absolute ethanol for 2 h to ensure the full wetting of solvent to the membrane,[19] and HI was then added to the solvent for further reduction. The reduction was performed at 40 ℃ for 24 h to completely reduce the GO membrane. After being thoroughly washed using ethanol to remove the adsorbed HI, $I_2$, and the residual solvent, the rGO membranes were dried in an oven at 40 ℃ for 24 h. The resultant rGO membranes obtained in water and ethanol solvents are denoted as rGO-water and rGO-ethanol, respectively. Both membranes exhibit a dark, smooth surface and possess a high degree of flexibility (Figure S4). X-ray photoelectron spectroscopy measurement (Figure S5 and Table S1) demonstrates similar surface chemistry

between rGO-water and rGO-ethanol membranes. Both rGO membranes show a relatively high reduction degree with a C/O ratio of ~6 after the reduction of HI at 40 ℃ for 24 h, agreeing well with the previous reports.[20]

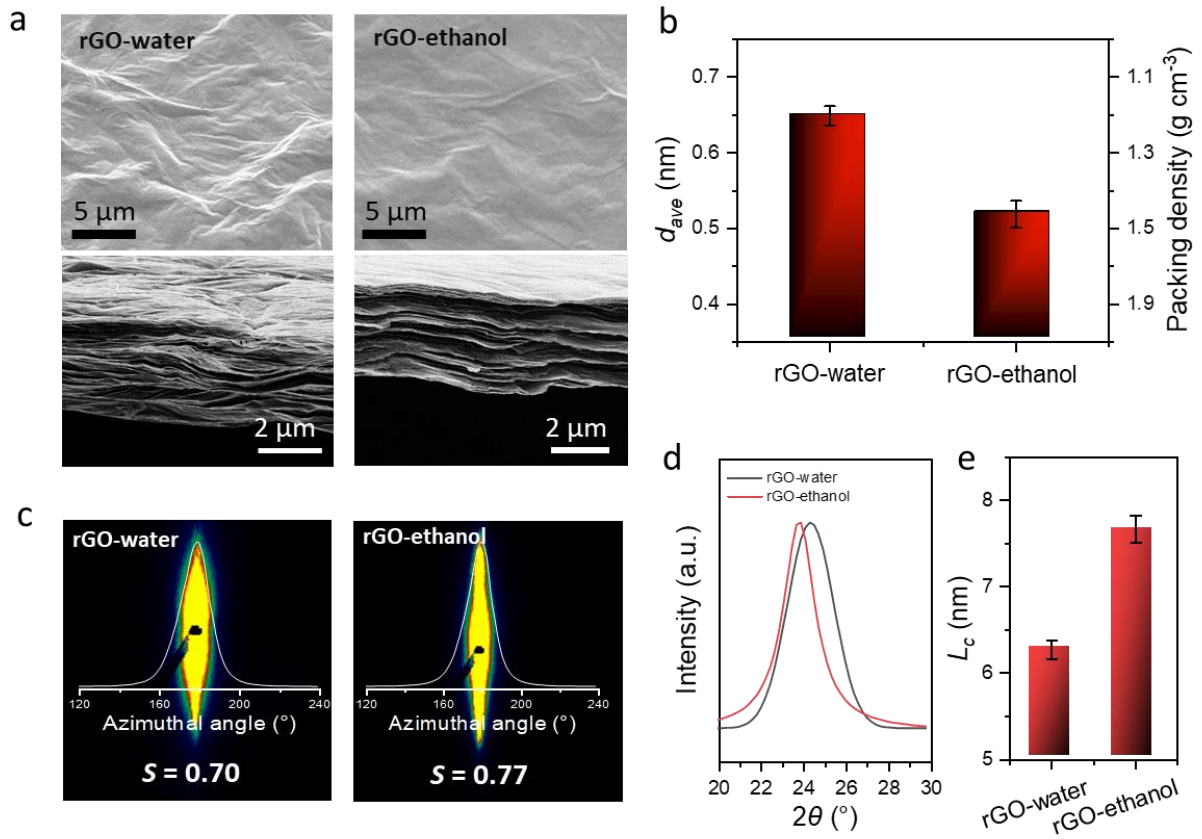


**Figure 2.** Structural characterization of rGO-water and rGO-ethanol. SEM images of the surface (top) and cross-sectional area (bottom) of rGO-water, rGO-ethanol. (b) Comparison of the packing density and average interlayer spacing ($d_{ave}$). (c) Scattering pattern obtained from the Synchrotron-based small-angle X-ray scattering with the incident beam passing through the cross-section of the membrane. Insert is the plot of the azimuthal dependence of the scattering intensity with the orientation distribution factor *S*. (d) Comparison of XRD patterns. (e) Stacking height ($L_c$) of graphitized clusters obtained from the XRD pattern by Scherrer equation.

We characterized the microstructure and nanotextures of rGO-water and rGO-ethanol membranes using various techniques. As shown in Figure 2a, the scanning electron microscopy (SEM) images of the top and cross-sectional area of the two rGO membranes indicates that the rGO membranes both have laminated stacking structure but show different surface morphologies and interlayer structures. In specific, the rGO-water exhibits a rougher surface and is more loosely stacked than the rGO-ethanol, resulting in a lower packing density (1.16 *vs.* 1.46 g $cm^{-3}$, Figure 2b). Correspondingly, the rGO-water shows a larger average interlayer spacing ($d_{ave}$) than rGO-ethanol (0.65 vs. 0.52 nm, Figure 2b), as estimated by its relative density to the graphite (see Method).[21] More insights into the nanotexture of these rGO membranes were obtained by small-angle X-ray scattering (SAXS). As shown in Figure 2c, the rGO-water shows a wider scattering pattern than the rGO-ethanol, suggesting a lower degree of sheet alignment. The degree of alignment was further quantified by plotting the azimuthal intensity distribution (insert in Figure 2c) and correlating it to the orientation distribution coefficient, *S*, by Hermans' distribution function.[22] A smaller value of *S* (0.7) observed in the rGO-water membrane compared to the rGO-ethanol membrane (0.77) confirms less orderly aligned nanosheets in the rGO-water, agreeing well with the more wrinkled and rougher surface morphologies of the rGO-water membrane (Figure 2a). The X-ray diffraction (XRD) pattern of both the rGO-water and rGO-ethanol membranes shows one diffraction peak at approximately 25°, suggesting the presence of one type of ordered structural unit (graphitized cluster) in both rGO membranes (Figure 2d). Notably, the rGO-water membrane exhibits a much wider diffraction peak than the rGO-ethanol membrane, corresponding to a smaller size of the graphitized cluster ($L_c$) in the rGO-water (6.17 *vs.* 7.50 nm) (Figure 2e). This observation indicates that the rGO nanosheets reduced in water have less propensity to restack, resulting in smaller graphitized crystals in the rGO-water membrane. The result can also

be confirmed by Raman spectrum analysis (Figure S7). From the analysis, rGO-water displays a stronger *D″* band compared to rGO-ethanol. Since it is well-established that the *D″* band is directly correlated with the amorphous phase of GO and rGO,[23] the larger area of the *D″* band provides further evidence for the smaller graphitized crystallinity of rGO reduced in water compared to ethanol.

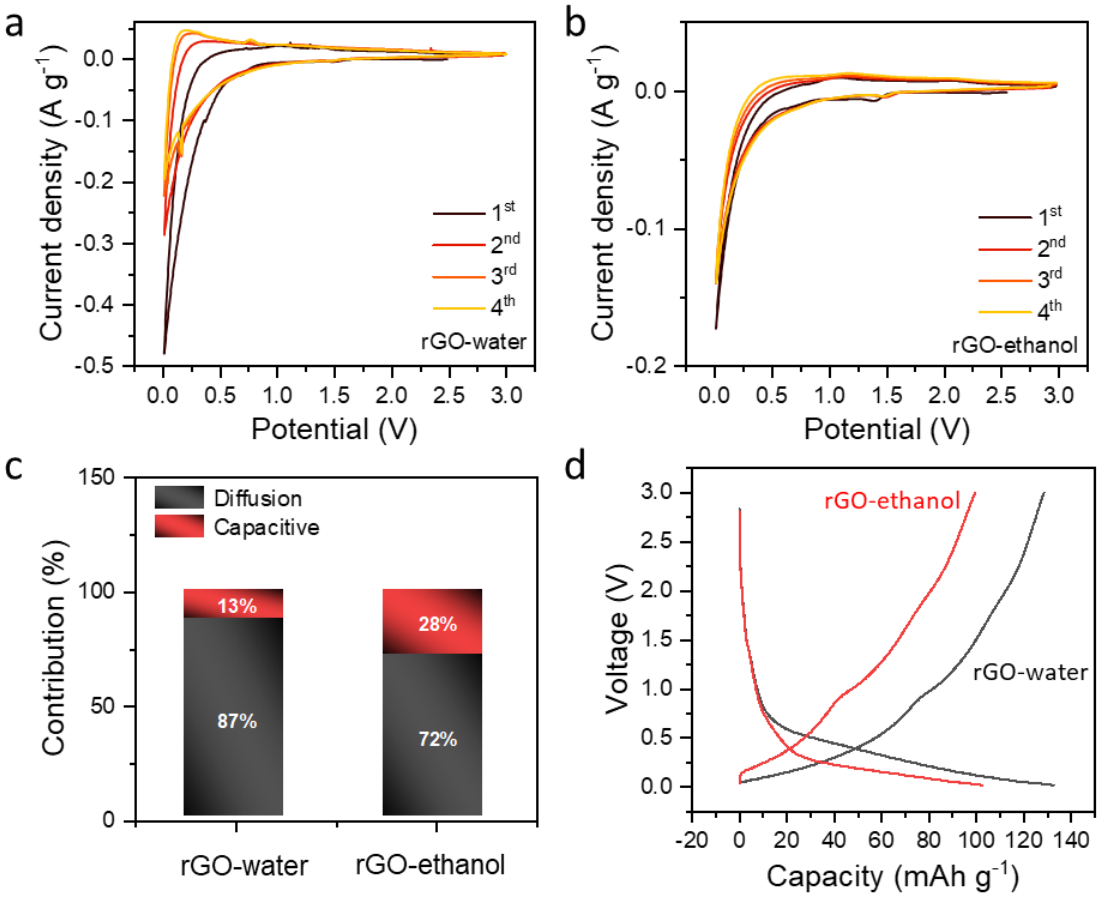


**Figure 3.** Electrochemical characterization of rGO-water and rGO-ethanol in the configuration of half coin cells with 1.0 M $LiPF_6$ as electrolyte and Lithium foil as the counter and reference electrodes. (a-b) First five cycles of cyclic voltammetry (CV) curves of rGO-water (a) and rGO-ethanol (b) at a scan rate of 0.1 mV $s^{-1}$. (c) Comparison of capacitive and diffusion-controlled

contributions at a scan rate of 0.1 mV $s^{-1}$. (d) Charge-discharge curves in the 25$^{th}$ cycle between 3.0 and 0.01 V at a current density of 0.1 A $g^{-1}$.

The different nanotextural formation between rGO-water and rGO-ethanol membranes was further revealed by the electrochemical characterization of the rGO membranes/Li half-cell (see experimental details). As shown in Figures 3a and 3b, the cells based on both rGO-water and rGO-ethanol membranes exhibit a nearly negligible cathodic current until the potential is below ~0.5 V *vs.* $Li/Li^+$. The CV curve of the rGO-water membrane-based cell shows the highest cathodic current near 0.01 V *vs.* $Li/Li^+$. Such a significant current increment under ~0.5 V could be attributed to the intercalation of $Li^+$ into the stacked graphene membrane to form layered compounds (i.e., $Li_xC$). In the anodic process, the CV curve of the rGO-water membrane-based cell exhibits a broad peak near ~ 0.2 V in the subsequent scans, which corresponds to the process of $Li^+$ extraction from the graphene stacks. In contrast, the CV curves of the cell based on the rGO-ethanol membrane show no obvious anodic peaks and small current through the potential window (0.01~3 V), indicative of less intercalation and de-intercalation of $Li^+$ ions in the graphitized region during the charging/discharging process. In addition, the CV curve of the rGO-water membrane-based cell displays an enormous loss of the initial current in the subsequent scan compared to that based on the rGO-ethanol. The prominent irreversible current loss in the CV curve of the rGO-water membrane-based cell at the 1$^{st}$ cycle can be attributed to the formation of the so-called solid electrolyte interphase and the possible trapping of $Li^+$ in its defect and wrinkled sites.[24] These observations align well with the microstructure characterization that the rGO-water exhibits a more pronounced wrinkled, defected and less graphitized structure compared to rGO-ethanol. Moreover, the electrochemical kinetic analysis shown in Figure 3c reveals the higher diffusion-controlled contribution of capacity in the rGO-water membrane-based cell (87% at 0.1 mV $s^{-1}$) compared

with that in the rGO-ethanol membrane-based cell (72% at 0.1 mV $s^{-1}$) (see Figures S8 and S9 for more information), agreeing well with the more obvious Li-ion intercalation observed in CV curve.

To further understand the Li-ion intercalation behavior in the rGO-water membrane, we analyzed the charge-discharge curves at 0.01-3.0 V with a current density of 0.1 A $g^{-1}$. As shown in Figure 3d, the discharge curve of the rGO-water membrane-based cell shows a plateau feature below 0.5 V while the discharge curve of the rGO-ethanol membrane-based cell shows no obvious plateau until the potential reaches below 0.25 V. We further plotted the differential capacity curves ($d$Q/$dV$) to allow the identification of the lithiation and de-lithiation peak. In comparison with the $dQ/dV$ curve of the rGO-ethanol membrane-based cell, the $dQ/d$V curve of the rGO-water membrane-based cell shows a stronger peak at a higher intercalation potential (0.48 vs. 0.17 V), indicating a lower energy barrier for Li-ion intercalation (Figure S10). In addition, the voltage polarization between the lithiation and delithiation peaks indicates the kinetics of charging and discharging.[25] Such a smaller value in rGO-water (0.47 V) further demonstrates the faster ion kinetics for Li-ion storage. We deemed that the presence of a more wrinkled structure in the rGO-water and the smaller graphitized cluster size may account for the favorable Li-ion intercalation and the higher Li-storage capacity but severe irreversibility at the first cycle than that of the rGO-ethanol. These electrochemical results further suggest the distinct nanotexture between the rGO-water and rGO-ethanol membranes.

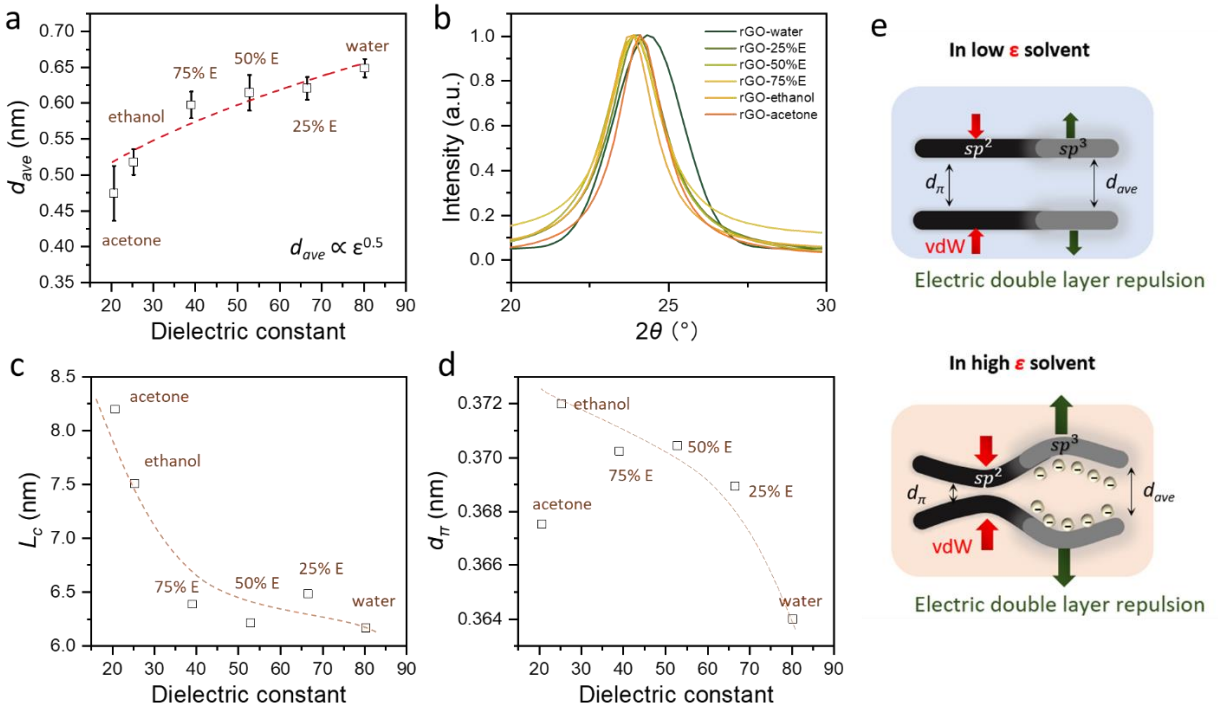


**Figure 4.** Characterization of the rGO membrane prepared from the solvent of different polarity. (a) The plot of $d_{ave}$ as a function of the dielectric constant of the solvent (empty dots). The fit with $d_{ave} \propto \varepsilon^{0.5}$ (dashed curve). (b) XRD spectra. The plot of $L_c$ (c) and $d_\pi$ (d) as a function of the dielectric constant of the solvent. (e) The proposed mechanism for the solvent effect on the nanotexture formation of GO membrane reduced by HI. The increased dielectric constant of the solvent aggravates the unevenly distributed sheet interactions across the nanosheets, thus promoting wrinkling formation.

Both the X-ray scattering measurement and electrochemical characterization demonstrate the significantly different interlayer nanotexture of rGO-water and rGO-ethanol membranes, suggesting the influence of the solvent on the nanotextural changes of GO membrane reduced by HI. We ascribe such kind of influences to the interaction between nanosheets which is altered by the solvent. In the realm of colloid and interface science, the typical Derjaguin-Landau-Verwey-Overbeek (DLVO) theory has been demonstrated to be capable of capturing the interaction of

nanoscale building blocks, such as graphene, carbon nanotubes, and clay particles in a wide range of polar media.[19,26,27] According to the theory, the interactions of two adjacent nanosheets are mainly determined by the attractive van der Waals (vdW) and repulsive electrical double-layer interactions. Many studies have demonstrated that these two types of interactions between the nanosheets are influenced by the surrounding solvent in terms of the polarity of the solvent (characterized by the dielectric constant, $\varepsilon$).[13,26] We thus hypothesize that such solvent effect on the nanotexture could be attributed to the polarity of the solvent.

We perform the chemical reduction on solvents with different polarity by employing a series of solvents including a mixed solvent of water and ethanol with the volume ratio of ethanol in 0% (pure water), 25% (25% E), 50% (50% E), 75% (75% E) and 100% (pure ethanol), as well as pure acetone with varied dielectric constant ranging from 80.3 to 20.7 (Table S2). As shown in Figure 4a, a gradual increase of the $d_{ave}$ from 0.47 to 0.65 nm is observed with the increase of the dielectric constant of the solvent. This observation corresponds to the formation of a more loosely stacked structure in the as-prepared membranes. A decrease in sheet alignment is supported by the 2D scattering pattern (Figure S11) Meanwhile, the XRD patterns (Figure 4b) illustrate different graphitic stacking units formed in the membrane prepared from different solvents. As shown in Figures 4c and 4d, an increase in the dielectric constant of the solvent gives rise to a gradual decrease of the graphitic cluster size ($L_c$) and a decrease of spacing ($d_\pi$) therein. Such a monotonic relationship of the nanotexture with the dielectric constant of the solvent confirms that the solvent effect, to some extent, is related to the polarity of the solvent.

Interestingly, we also find that the above relationships can be well described by the DLVO theory framework. Specifically, the ionization of functional groups (which is the main source of negative charges on GO nanosheets) leads to electrical double-layer repulsion between two GO

nanosheets, resulting in their separation. The length scales of this repulsive force can be described by the Debye length ($\kappa^{-1}$), which is scaled with the dielectric constant of the surrounding solvent ($\varepsilon$), $\kappa^{-1} \propto \varepsilon^{0.5}$ (see Supplementary Notes 1). Such a relationship fits well with our results ($d_{ave} \propto \varepsilon^{0.5}$) with the determination of coefficient ($R^2$) > 0.925 (Figure 4a). This observation indicates that electrical double-layer repulsion is the dominant force in the increase of the interlayer distance of the rGO membrane reduced in solvents with higher polarity. Similar correlation behavior was also observed in previous studies on the equilibrium interlayer spacing of two adjacent GO nanosheets to the thickness of the repelling double layers.[13,28] However, it should be noted that such linear relationships between the channel size and dielectric constant may not be applicable in other organic solvents when the dielectric constant is below a threshold and exceeds a certain value due to the change of the electrical double layer.[25,29]

The observation that the rGO-water membrane has the most loosely stacked structures, compared to other samples, is somewhat surprising. This is because rGO nanosheets, known for their hydrophobic nature, are often expected to restack and graphitize more readily in high-polarity solvents due to the strong van der Waals interactions. A plausible reason could be the non-evenly distributed sheet interactions as a result of the chemical inhomogeneity of the rGO nanosheets. Notably, GO intrinsically contains multiple sites of $sp^2$ (aromatic) and $sp^3$ (aliphatic) hybridized carbon domains throughout the entire nanosheet.[30,31] Although a gradual change in C/O is observed from the macroscopic level during the conversion of GO to rGO, a microscopically inhomogeneous chemical conversion occurs with the edge of the $sp^2$ domain progressively propagating to the $sp^3$ carbon matrix. As such, the resultant rGO nanosheets contain the mixed components of $sp^2$- and $sp^3$-hybridized carbon regions across the plane.[30] The chemical differences enable two types of domains to be dominated by different interactions. As sketched in Figure 4e,

the graphene-like $sp^2$ domain is more vulnerable to vdW attraction, which increases with increasing ε of the solvent (see Supplementary Notes 1 Notes 1). Hence, the reduction conducted in the higher polarity solvent promotes the aggregation of the $sp^2$ regions of the nanosheets by enhancing the vdW interaction. This is consistent with the observed decrease in $d_\pi$ in the graphitized clusters formed in higher polarity solvent (Figure 4d). Meanwhile, the oxygen-rich $sp^3$ regions on rGO nanosheets are found to be predominantly affected by electrical double-layer repulsion owing to the ionization of the carboxyl and hydroxyl groups. The increment of ε of solvent provides a more appropriate environment for ionizing the functional group and thickening the repulsive double-layer and therefore shows a growing repulsive interactive behavior. As such, increasing the solvent polarity could enhance both the attractive vdW interactions of the $sp^2$ domains and the repulsive electrical double-layer interactions of the $sp^3$ domains. Such enhancement of the opposite interaction exerted in the different portions of the nanosheet largely account for the severe nanowrinkling formation and low-packing assembly in the rGO obtained in a highly polar solvent.

While we have demonstrated a correlation between the dielectric constant of the solvent used in this experiment with the nanotexture formation of the rGO membrane, it is worth noting that other solvent effects, especially when water is involved, may also play a role. For example, the hydrogen bonding formed between the water-water and water- GO nanosheet,[32] the role of dielectric constant in variability in ionic strength in different electrolyte and solvation layers around charged functional groups,[33] the solvation forces originated from the arrangement of the solvent molecules near the graphene surface could co-contributes to the observed nanotextures.[34] Desipte that our study underscores the primary role of solvent polarity in the nanotexture formation, further

investigations are needed to delve into the precise mechanisms of these additional interactions with water and their potential synergy with polarity-driven effects.

## Conclusion

The solvent involved in wet-chemical processes notably influences the formation of nanotextures in 2D laminar membranes. Our investigation of HI-rGO membranes prepared from water, ethanol, and their mixtures revealed a correlation between the dielectric constant of the solvent and the extent of nanowrinkling of the membranes. This effect can be attributed to the enhanced discrepancies between repulsive interactions in oxygen-rich regions and attractive interactions in graphene-like regions on the nanosheets. Our study emphasizes the importance of considering solvent effects in future research and highlights the potential of solvent engineering as an effective strategy for controlling the structure of 2D laminar membranes. Given the increasing interest in tailoring the 2D nanochannel structure for applications involving the transport of ions, molecules, and electrons,[35–37] such as water purification, energy storage, and flexible electronics, we hope that the solvent effect highlighted in this study will serve as a catalyst for further research into harnessing these "weak" non-covalent interactions to engineer the nanotexture of graphene and other 2D materials.

## EXPERIMENTAL METHODS

**Preparation of GO membranes.** The graphite oxide used in this work was prepared from natural graphite (Sigma-Aldrich) by modified Hummer's method.[38] Then, the as-synthesized graphite oxide was suspended in water and dialysis to remove any remaining salt and acids. After purification, the graphite oxide was diluted to 0.5 mg $mL^{-1}$ and then ultrasonicated using Branson Digital Sonifier (S450D, 450W, 30% amplitude) for 30 mins in the ice-water bath to obtain GO

dispersion. The GO membrane was made by filtration of 30 mL of the above GO dispersion on a polycarbonate (47 mm in diameter, 0.1 μm pore size) for 24 h to make a dried membrane. The as-prepared GO membrane was then cut into small pieces with a diameter of 0.6 cm for the following reduction procedure.

**Preparation of solvent-mediated rGO membranes.** GO membranes were placed in 3 mL solvent and immersed for 2 hours before reduction. This deliberate duration ensured sufficient time for the solvent including the mixed solvent to fully penetrate in GO flakes and facilitate uniform and complete wetting of the GO membrane.[39] Then, 1.0 mL HI (47 wt.%) was added to the solvent. The reduction reaction was conducted at 40 °C for 24 h in an oven. After reduction, the rGO membrane was thoroughly washed with ethanol until the washed residue showed no colors to ensure that the by-products ($I_2$ and HI) were removed. The resultant wet rGO membrane was then sandwiched by glass slides and placed in an oven at 40 °C for 24 hrs to yield a series of dry membranes named rGO-*X* (*X* represents the type of solvent used for reduction, i.e., rGO-ethanol).

The dielectric constant (ε) of a mixed solvent can be estimated from the following equation:[40]

$$\ln(\varepsilon_m) = \varphi_1 \ln(\varepsilon_1) + \varphi_2 \ln(\varepsilon_2)$$

in which, φ represents the volume fraction of a particular solvent.

**Characterization of solvent-mediated rGO membranes.** The estimation of average interlayer spacing ($d_{ave}$) follows the literature previously reported:[21]

$$d_{ave} = \frac{Area\ density\ of\ graphene}{Packing\ density\ of\ rGO\ membranes}$$

where the area density of graphene was 0.77 mg $cm^{-2}$.

The packing density of the membrane was determined by the mass-to-volume ratio. The mass of the membrane was measured by averaging the mass of four pieces of the membrane on balance (HR-250AZ). The volume of the membrane was calculated by its diameter and thickness. The

thickness is measured by averaging four pieces of a sample, each measured three times using an RS PRO micrometer.

X-ray diffraction was performed on a Bruker D8 Advance diffractometer with Cu Kα radiation ($\lambda = 1.5406$ Å). The sample was attached to the zero-background plate, and all parts were transferred to the sample holder for measurement. The scans were taken at a step size of 0.01° in the range of 5-35°. The analysis of XRD data followed our previous work to obtain the graphitized stacking height ($L_c$) using the following equation.[41]

$$L_c = \frac{0.89\,\lambda}{FWHM(2\theta)cos\theta}$$

where *FWHM(2θ)* is the full width of half maximum of the diffraction peak.

Raman spectroscopy was conducted on a Renishaw inVia Raman microscope using a 532 nm laser with a power of 1 mW. The peak deconvolution of the Raman spectra was based on the work reported by Claramunt *et al*. and Malard *et al*.[23,42] The helium ion microscope was conducted on a Zeiss ORION NanoFab to probe the surface morphologies of the membranes.

Synchrotron-based SAXS was conducted at Australia Synchrotron to measure the sheet alignment and morphology. The data were collected with the incident beam perpendicularly passing through the surface and the edge of the membrane. The beam was adjusted to 20 keV at a camera length of 746 mm and 8.2 keV at a camera length of 7396 mm to probe the scattering vector ($q$) ranging from $2\times10^{-3}$ Å$^{-1}$ to 2 Å$^{-1}$. The alignment of the nanosheets can be inferred from the orientation distribution coefficient, $S$, calculated by the following equation:[22]

$$S = \frac{1}{2}(3\langle cos^2\varphi\rangle - 1)$$

where $\langle cos^2\varphi \rangle$ is the average cosine square weighted by the azimuthal intensity $I(\varphi)$ from the scattering pattern:

$$\langle cos^2\varphi \rangle = \frac{\int_0^{2\pi} I(\varphi) cos^2\varphi \, sin\varphi \, d\varphi}{\int_0^{2\pi} I(\varphi) \, sin\varphi \, d\varphi}$$

A perfect alignment along the $\varphi = 0°$ and $90°$ directions corresponds to $S = 1$ and -0.5, respectively, and a completely random orientation corresponds to $S = 0$. All data processing was conducted on scatterbrain (V2.82) and the Irena/Nika package (V2.7) in the IgorPro8 environment.[43,44]

**Electrochemical measurement.** The solvent-mediated rGO membranes were pre-immersed in 1.0 M electrolyte for 20 min under vacuum conditions and then transferred into the glovebox overnight to allow the electrolyte to fully permeate to the nanochannels. Then, the membranes were assembled into Li/MGM *CR 2016* half coin-type cells in a glove box with Li foil as the counter electrode, Whatman$^{@R}$ GF/F glass microfibers (thickness of 0.42 mm) as the separator, and 100 µl of 1.0 M $LiPF_6$ in a mixture of EC and EMC (1:1 v/v) (Sigma-Aldrich). Cyclic voltammetry was performed at scan rates of 0.1, 0.5, 1, 2, and 5 mV s-1 with each scan rate for 4 cycles. The galvanostatic charge-discharge (GCD) curves were taken on the LAND Battery Testing System (CT3001A) in the 0.05 -3.0 V range (vs. $Li/Li^+$) at current densities of 50, 100, 200, 500, and 1000 mA $g^{-1}$, respectively.

The differentiation of the capacitance contribution was conducted on CV curves according to Dunn's method.[45] This analysis allows us to distinguish and quantify the capacitance contribution from the capacitive process and diffusion-controlled process separately. This method is based on the knowledge that the current density $i(V)$ at a given voltage is the sum of the capacitive contribution ($k_1 v$) and diffusion-controlled contribution ($k_2 v^{0.5}$), expressed as

$$i(V) = k_1 v + k_2 v^{0.5}$$

where $k_1$ is the capacitive factor, $k_2$ is the diffusion-controlled factor, and $v$ represents the scanning rate (mV $s^{-1}$) for the measurement being conducted.

By converting the questions to

$$i(V)/v^{0.5} = k_1 v^{0.5} + k_2$$

$k_1$ and $k_2$ at a given V can be extrapolated from the plot of $i(V)/v^{0.5}$ ***vs.*** $v^{0.5}$ as the slope and interception, respectively, via linear fitting. After that, the capacitive contribution of the current density at a specific V can be obtained by $k_1 v$. For the following analysis, 500 voltage points are selected uniformly from the CV curve in the potential window of (-0.5 to 5 V) to extrapolate the capacitive contribution to the current density, and the corresponding enclosed area gives the non-diffusion-controlled capacitance.

ASSOCIATED CONTENT

**Supporting Information**. The following files are available free of charge. Surface chemistry characterization, Raman spectroscopy; Additional electrochemical characterization, (PDF)

AUTHOR INFORMATION

Corresponding Author:

*E-mail: qhliang@gia.cas.cn; dan.li1@unimelb.edu.au;

Author Contributions

Y.C. carried out experiments and analyzed the data. L.Z. performed electrochemical measurements. X.D. helped with the schematic drawing. Y.C. wrote the manuscript with constructive contributions from Q.L., G.V.F., and D.L. Q. L. and D. L. co-supervised this project. All authors were involved in the discussion of this work.

Notes

The authors declare no competing financial interests.

ACKNOWLEDGMENT

This work was supported by the Australia Research Council (FL180100029, DP220103498, IC180100049, DE190100445). The authors thank Australia Synchrotron for access to the Small/Wide X-ray scattering beamline through proposals of M14459 and M17715. XRD and Raman tests were performed in the Materials Characterization and Fabrication platform at the University of Melbourne. XPS was carried out at the X-ray platform at Monash University.

REFERENCES

(1) Jeong, G. H.; Sasikala, S. P.; Yun, T.; Lee, G. Y.; Lee, W. J.; Kim, S. O. Nanoscale Assembly of 2D Materials for Energy and Environmental Applications. *Adv. Mater.* **2020**, *32* (35), 1907006. https://doi.org/10.1002/adma.201907006.

(2) Li, C.; Meckler, S. M.; Smith, Z. P.; Bachman, J. E.; Maserati, L.; Long, J. R.; Helms, B. A. Engineered Transport in Microporous Materials and Membranes for Clean Energy Technologies. *Adv. Mater.* **2018**, *30* (8), 1704953. https://doi.org/10.1002/adma.201704953.

(3) Yang, H.; Zhang, X.; Yang, J.; Bo, Z.; Hu, M.; Yan, J.; Cen, K. Molecular Origin of Electric Double-Layer Capacitance at Multilayer Graphene Edges. *J. Phys. Chem. Lett.* **2017**, *8* (1), 153–160. https://doi.org/10.1021/acs.jpclett.6b02659.

(4) Cheng, C.; Li, D. Solvated Graphenes: An Emerging Class of Functional Soft Materials. *Adv. Mater.* **2013**, *25* (1), 13–30. https://doi.org/10.1002/adma.201203567.

(5) Pei, S.; Zhao, J.; Du, J.; Ren, W.; Cheng, H.-M. Direct Reduction of Graphene Oxide Films into Highly Conductive and Flexible Graphene Films by Hydrohalic Acids. *Carbon* **2010**, *48* (15), 4466–4474. https://doi.org/10.1016/j.carbon.2010.08.006.

(6) Su, Y.; Kravets, V. G.; Wong, S. L.; Waters, J.; Geim, A. K.; Nair, R. R. Impermeable Barrier Films and Protective Coatings Based on Reduced Graphene Oxide. *Nat. Commun.* **2014**, *5* (1), 4843. https://doi.org/10.1038/ncomms5843.

(7) Cao, Y.; Xiong, Z.; Liang, Q.; Jiang, W.-J.; Xia, F.; Du, X.; Zu, L.; Mudie, S.; Franks, G. V.; Li, D. Subnanometric Stacking of Two-Dimensional Nanomaterials: Insights from the Nanotexture Evolution of Dense Reduced Graphene Oxide Membranes. *ACS Nano* **2023**, *17* (5), 5072–5082. https://doi.org/10.1021/acsnano.3c00155.
(8) Agarwal, V.; Zetterlund, P. B. Strategies for Reduction of Graphene Oxide – A Comprehensive Review. *Chem. Eng. J.* **2021**, *405*. https://doi.org/10.1016/J.CEJ.2020.127018.
(9) Yin, K.; Feng, N.; Godbert, N.; Xing, P.; Li, H. Self-Assembly of Cholesteryl Carbon Dots with Circularly Polarized Luminescence in Solution and Solvent-Free Phases. *J. Phys. Chem. Lett.* **2023**, *14* (4), 1088–1095. https://doi.org/10.1021/acs.jpclett.2c03829.
(10) Sun, Y. W.; Papageorgiou, D. G.; Humphreys, C. J.; Dunstan, D. J.; Puech, P.; Proctor, J. E.; Bousige, C.; Machon, D.; San-Miguel, A. Mechanical Properties of Graphene. *Appl. Phys. Rev.* **2021**, *8* (2), 021310. https://doi.org/10.1063/5.0040578.
(11) Wang, Y.; Wang, S.; Li, P.; Rajendran, S.; Xu, Z.; Liu, S.; Guo, F.; He, Y.; Li, Z.; Xu, Z.; Gao, C. Conformational Phase Map of Two-Dimensional Macromolecular Graphene Oxide in Solution. *Matter* **2020**, *3* (1), 230–245. https://doi.org/10.1016/j.matt.2020.04.023.
(12) Zhang, M.; Li, P.; Li, M.; Zheng, W.; Xie, G.; Xu, X.; Liu, C.; Jia, J. Controlling Assembly Behaviors of Laminar GO Membranes in Organic Solvents by Altering GO-Solvent Interactions. *J. Membr. Sci.* **2021**, *640*, 119841. https://doi.org/10.1016/j.memsci.2021.119841.
(13) Akbari, A.; Meragawi, S. E.; Martin, S. T.; Corry, B.; Shamsaei, E.; Easton, C. D.; Bhattacharyya, D.; Majumder, M. Solvent Transport Behavior of Shear Aligned Graphene Oxide Membranes and Implications in Organic Solvent Nanofiltration. *ACS Appl. Mater. Interfaces* **2018**, *10* (2), 2067–2074. https://doi.org/10.1021/acsami.7b11777.
(14) Yang, Q.; Su, Y.; Chi, C.; Cherian, C. T.; Huang, K.; Kravets, V. G.; Wang, F. C.; Zhang, J. C.; Pratt, A.; Grigorenko, A. N.; Guinea, F.; Geim, A. K.; Nair, R. R. Ultrathin Graphene-Based Membrane with Precise Molecular Sieving and Ultrafast Solvent Permeation. *Nat. Mater.* **2017**, *16* (12), 1198–1202. https://doi.org/10.1038/nmat5025.
(15) Ramakrishna, T. R. B.; Mathesh, M.; Liu, Z.; Zhang, C.; Du, A.; Liu, J.; Barrow, C. J.; Chen, M.; Biggs, M. J.; Yang, W. Solvent Effect on Supramolecular Self-Assembly of Chlorophylls a on Chemically Reduced Graphene Oxide. *Langmuir* **2020**, *36* (45), 13575–13582. https://doi.org/10.1021/acs.langmuir.0c02370.
(16) Lv, W.; Zhang, C.; Li, Z.; Yang, Q. H. Self-Assembled 3D Graphene Monolith from Solution. *J. Phys. Chem. Lett.* **2015**, *6* (4), 658–668. https://doi.org/10.1021/jz502655m.
(17) Jiang, Y.; Xu, Z.; Huang, T.; Liu, Y.; Guo, F.; Xi, J.; Gao, W.; Gao, C. Direct 3D Printing of Ultralight Graphene Oxide Aerogel Microlattices. *Adv. Funct. Mater.* **2018**, *28* (16), 1707024. https://doi.org/10.1002/adfm.201707024.
(18) Qin, M. M.; Ji, W.; Feng, Y. Y.; Feng, W. Transparent Conductive Graphene Films Prepared by Hydroiodic Acid and Thermal Reduction. *Chin. Phys. B* **2014**, *23* (2), 3–8. https://doi.org/10.1088/1674-1056/23/2/028103.
(19) Zheng, S.; Tu, Q.; Wang, M.; Urban, J. J.; Mi, B. Correlating Interlayer Spacing and Separation Capability of Graphene Oxide Membranes in Organic Solvents. *ACS Nano* **2020**, *14* (5), 6013–6023. https://doi.org/10.1021/acsnano.0c01550.
(20) Zhang, M.; Wang, Y.; Huang, L.; Xu, Z.; Li, C.; Shi, G. Multifunctional Pristine Chemically Modified Graphene Films as Strong as Stainless Steel. *Adv. Mater.* **2015**, *27* (42), 6708–6713. https://doi.org/10.1002/adma.201503045.

(21) Yang, X.; Cheng, C.; Wang, Y.; Qiu, L.; Li, D. Liquid-Mediated Dense Integration of Graphene Materials for Compact Capacitive Energy Storage. *Science* **2013**, *341* (6145), 534–537. https://doi.org/10.1126/science.1239089.
(22) Hermans, J. J.; Hermans, P. H.; Vermaas, D.; Weidinger, A. Quantitative Evaluation of Orientation in Cellulose Fibres from the X-Ray Fibre Diagram. *Recl. Trav. Chim. Pays-Bas* **1946**, *65* (6), 427–447. https://doi.org/10.1002/recl.19460650605.
(23) Claramunt, S.; Varea, A.; López-Díaz, D.; Velázquez, M. M.; Cornet, A.; Cirera, A. The Importance of Interbands on the Interpretation of the Raman Spectrum of Graphene Oxide. *J. Phys. Chem. C* **2015**, *119* (18), 10123–10129. https://doi.org/10.1021/acs.jpcc.5b01590.
(24) An, S. J.; Li, J.; Daniel, C.; Mohanty, D.; Nagpure, S.; Wood, D. L. The State of Understanding of the Lithium-Ion-Battery Graphite Solid Electrolyte Interphase (SEI) and Its Relationship to Formation Cycling. *Carbon* **2016**, *105*, 52–76. https://doi.org/10.1016/J.CARBON.2016.04.008.
(25) Zhou, J.; Ma, K.; Lian, X.; Shi, Q.; Wang, J.; Chen, Z.; Guo, L.; Liu, Y.; Bachmatiuk, A.; Sun, J.; Yang, R.; Choi, J.; Rümmeli, M. H. Eliminating Graphite Exfoliation with an Artificial Solid Electrolyte Interphase for Stable Lithium-Ion Batteries. *Small* **2022**, 2107460. https://doi.org/10.1002/SMLL.202107460.
(26) Gudarzi, M. M. Colloidal Stability of Graphene Oxide: Aggregation in Two Dimensions. *Langmuir* **2016**, *32* (20), 5058–5068. https://doi.org/10.1021/acs.langmuir.6b01012.
(27) Missana, T.; Adell, A. On the Applicability of DLVO Theory to the Prediction of Clay Colloids Stability. *J. Colloid Interface Sci.* **2000**, *230* (1), 150–156. https://doi.org/10.1006/jcis.2000.7003.
(28) Gao, W.; Alemany, L. B.; Ci, L.; Ajayan, P. M. New Insights into the Structure and Reduction of Graphite Oxide. *Nat. Chem.* **2009**, *1* (5), 403–408. https://doi.org/10.1038/NCHEM.281.
(29) Brindley, G. W. Intracrystalline Swelling of Montmorillonites in Water-Dimethylsulfoxide Systems. *Clays Clay Miner.* **1980**, *28* (5), 369–372. https://doi.org/10.1346/CCMN.1980.0280506.
(30) Mattevi, C.; Eda, G.; Agnoli, S.; Miller, S.; Mkhoyan, K. A.; Celik, O.; Mastrogiovanni, D.; Granozzi, G.; Carfunkel, E.; Chhowalla, M. Evolution of Electrical, Chemical, and Structural Properties of Transparent and Conducting Chemically Derived Graphene Thin Films. *Adv. Funct. Mater.* **2009**, *19* (16), 2577–2583. https://doi.org/10.1002/adfm.200900166.
(31) Zhang, Q.; Zheng, H.; Geng, Z.; Jiang, S.; Ge, J.; Fan, K.; Duan, S.; Chen, Y.; Wang, X.; Luo, Y. The Realistic Domain Structure of As-Synthesized Graphene Oxide from Ultrafast Spectroscopy. *J. Am. Chem. Soc.* **2013**, *135* (33), 12468–12474. https://doi.org/10/f22ms5.
(32) Compton, O. C.; Cranford, S. W.; Putz, K. W.; An, Z.; Brinson, L. C.; Buehler, M. J.; Nguyen, S. T. Tuning the Mechanical Properties of Graphene Oxide Paper and Its Associated Polymer Nanocomposites by Controlling Cooperative Intersheet Hydrogen Bonding. *ACS Nano* **2012**, *6* (3), 2008–2019. https://doi.org/10.1021/nn202928w.
(33) Sarmini, K.; Kenndler, E. Ionization Constants of Weak Acids and Bases in Organic Solvents. *J. Biochem. Biophys. Methods* **1999**, *38* (2), 123–137. https://doi.org/10.1016/S0165-022X(98)00033-5.
(34) Israelachvili, J. N. Solvation, Structural, and Hydration Forces. In *Intermolecular and Surface Forces*; Elsevier, 2011; pp 341–380. https://doi.org/10.1016/B978-0-12-375182-9.10015-6.
(35) Gopinadhan, K.; Hu, S.; Esfandiar, A.; Lozada-Hidalgo, M.; Wang, F. C.; Yang, Q.; Tyurnina, A. V.; Keerthi, A.; Radha, B.; Geim, A. K. Complete Steric Exclusion of Ions and

Proton Transport through Confined Monolayer Water. *Science* **2019**, *363* (6423), 145–148. https://doi.org/10.1126/SCIENCE.AAU6771.
(36) Keerthi, A.; Geim, A. K.; Janardanan, A.; Rooney, A. P.; Esfandiar, A.; Hu, S.; Dar, S. A.; Grigorieva, I. V.; Haigh, S. J.; Wang, F. C.; Radha, B. Ballistic Molecular Transport through Two-Dimensional Channels. *Nature* **2018**, *558* (7710), 420–423. https://doi.org/10.1038/S41586-018-0203-2.
(37) Robin, P.; Emmerich, T.; Ismail, A.; Niguès, A.; You, Y.; Nam, G.-H.; Keerthi, A.; Siria, A.; Geim, A. K.; Radha, B.; Bocquet, L. Long-Term Memory and Synapse-like Dynamics in Two-Dimensional Nanofluidic Channels. *Science* **2023**, *379* (6628), 161–167. https://doi.org/10.1126/science.adc9931.
(38) Kovtyukhova, N.; Ollivier, P.; Martin, B.; Mallouk, T.; Chizhik, S.; Buzaneva, E.; Gorchinskiy, A. Layer-by-Layer Assembly of Ultrathin Composite Films from Micron-Sized Graphite Oxide Sheets and Polycations. *Chem. Mater.* **1999**, *11* (3), 771–778.
(39) Zheng, S.; Tu, Q.; Urban, J. J.; Li, S.; Mi, B. Swelling of Graphene Oxide Membranes in Aqueous Solution: Characterization of Interlayer Spacing and Insight into Water Transport Mechanisms. *ACS Nano* **2017**, *11* (6), 6440–6450. https://doi.org/10.1021/acsnano.7b02999.
(40) Jouyban, A.; Soltanpour, S.; Chan, H.-K. A Simple Relationship between Dielectric Constant of Mixed Solvents with Solvent Composition and Temperature. *Int. J. Pharm.* **2004**, *269* (2), 353–360. https://doi.org/10.1016/j.ijpharm.2003.09.010.
(41) Cao, Y.; Xiong, Z.; Xia, F.; Franks, G. V.; Zu, L.; Wang, X.; Hora, Y.; Mudie, S.; He, Z.; Qu, L.; Xing, Y.; Li, D. New Structural Insights into Densely Assembled Reduced Graphene Oxide Membranes. *Adv. Funct. Mater.* **2022**, *32* (42), 2201535. https://doi.org/10.1002/adfm.202201535.
(42) Malard, L. M.; Pimenta, M. A.; Dresselhaus, G.; Dresselhaus, M. S. Raman Spectroscopy in Graphene. *Phys. Rep.* **2009**, *473* (5–6), 51–87. https://doi.org/10.1016/j.physrep.2009.02.003.
(43) Ilavsky, J. Nika: Software for Two-Dimensional Data Reduction. *J. Appl. Crystallogr.* **2012**, *45* (2), 324–328. https://doi.org/10.1107/S0021889812004037.
(44) Ilavsky, J.; Jemian, P. R. Irena: Tool Suite for Modeling and Analysis of Small-Angle Scattering. *J. Appl. Crystallogr.* **2009**, *42* (2), 347–353. https://doi.org/10.1107/S0021889809002222.
(45) Augustyn, V.; Simon, P.; Dunn, B. Pseudocapacitive Oxide Materials for High-Rate Electrochemical Energy Storage. *Energy Environ. Sci.* **2014**, *7* (5), 1597–1614. https://doi.org/10.1039/c3ee44164d.

**TOC graph**

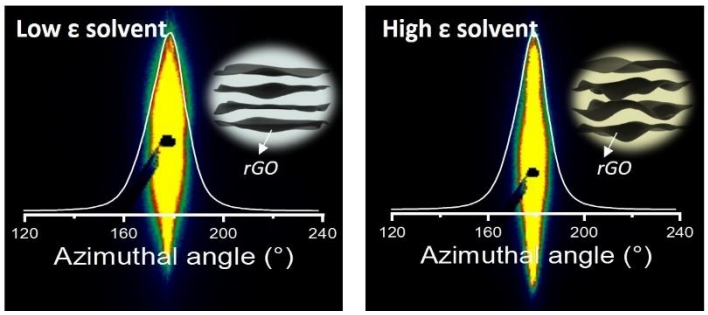
Low ε solvent
rGO
120
160
200
240
Azimuthal angle (°)
High ε solvent
rGO
120
160
200
240
Azimuthal angle (°)